Forced dynamic dewetting of structured surfaces: Influence of surfactants

Franziska Henrich,[1] Dorota Linke,[1] Hans Martin Sauer,[2] Edgar Dörsam,[2] Steffen Hardt,[3] Hans-Jürgen Butt,[1] and Günter K. Auernhammer[1,4,*]

[1]*Max Planck Institute for Polymer Research, Ackermannweg 10, 55128 Mainz, Germany*
[2]*Technische Universität Darmstadt, Institut für Druckmaschinen und Druckverfahren, Magdalenenstrasse 2, 64289 Darmstadt, Germany*
[3]*Technische Universität Darmstadt, Fachgebiet Nano- und Mikrofluidik, Alarich-Weiss-Straße 10, 64287 Darmstadt, Germany*
[4]*Leibniz Institut für Polymerforschung, Hohe Straße 6, 01069 Dresden, Germany*

(Received 4 September 2017; published 9 December 2019)

We analyze the dewetting of printing plates for gravure printing with well-defined gravure cells. The printing plates were mounted on a rotating horizontal cylinder that is half immersed in an aqueous solution of the anionic surfactant sodium 1-decanesulfonate. The gravure plates and the presence of surfactants serve as one example of a real-world dewetting situation. When rotating the cylinder, a liquid meniscus was partially drawn out of the liquid forming a dynamic contact angle at the contact line. The dynamic contact angle is decreased on a structured surface as compared to a smooth one. This is due to contact line pinning at the borders of the gravure cells. Additionally, surfactants tend to decrease the dynamic receding contact angle. We consider the interplay between these two effects. We compare the height differences of the meniscus on the structured and unstructured area as a function of dewetting speeds. The height difference increases with increasing dewetting speed. With increasing size of the gravure cells, this height difference and the induced changes in the dynamic contact angle increased. By adding surfactant, the height difference and the changes in the contact angle for the same surface decreased. We further note that although the liquid dewets the printing plates, some liquid is always left in the gravure cell. At high enough surfactant concentrations or high enough dewetting speed, the dynamic contact angles in the structured surface approach those in flat surfaces. We conclude that surfactant reduces the influence of surface structure on dynamic dewetting.

DOI: 10.1103/PhysRevFluids.4.124202

I. INTRODUCTION

Wetting and dewetting of solid surfaces play an important role in many natural and technological contexts, ranging from the movement of water drops on the wings of butterflies and birds [1,2], to printing [3,4] and cleaning. The latter is important in industrial processes, e.g., the manufacturing of chips on silicon wafers [5–8]. For an optimal performance of any of these processes, a fundamental understanding of the wetting properties is essential.

For simple liquids on flat surfaces, some understanding of static and dynamic wetting has been achieved [3,9–11]. The contact angle at the three-phase contact line (contact line in short), where liquid, substrate, and gas (or a second liquid) meet, is a very convenient parameter to characterize the wetting behavior. In the static case, two contact angles have to be distinguished: the static advancing

*auernhammer@ipfdd.de

contact angle θ_a, and the static receding contact angle θ_r. These contact angles are unique properties of the specific substrate and the liquid-gas or liquid-liquid combination. For moving contact lines, dynamic aspects have to be considered in addition to that. Several theories explain the dynamic contact angle as a function of wetting or dewetting speed of the contact line on various length scales. Two prominent examples are the molecular kinetic theory [12,13] or the hydrodynamic theory [14–16]. A detailed description and comparison of the theories can be found in recent review articles [3,9] .

These modeling attempts went hand in hand with a wealth of experimental work on the wetting behavior of single-component liquids [3,9,17]. Also, simulations on the wetting of single-component liquids have been executed [10,18,19]. However, the dynamic wetting of multicomponent liquids, like surfactant solutions, is less understood. In recent years, an increasing amount of research has been done on this topic [3,20–27]. Surfactant molecules absorb at the interface and change the interfacial tension [28]. Flow-induced heterogeneities of the absorbed surfactant layer at the interface also influence the dynamic behavior of the liquid. Concentration gradients at the interface lead to Marangoni stresses that change the hydrodynamic boundary condition [22,23] or the flow profile inside the liquid [24,29]. The majority of the studies investigate spontaneous wetting, e.g., the spontaneous spreading of drops. Less investigated is the forced wetting behavior, e.g., wetting and dewetting with a prescribed speed of the contact line. In the latter case, liquid moves over a solid surface due to external forces.

Previous work shows that surfactants influence the wetting behavior even well below the critical micelle concentration (CMC) [24–27,30,31]. All of these studies have been performed on relatively smooth surfaces. However, in many technical wetting applications, the surfaces are not smooth but have a topography. Therefore, the following question arises: How do surface structures influence the effect of surfactants on dynamic dewetting? Forced dewetting on structured surfaces has not been intensely studied so far [32–35].

In many technical processes (like printing processes), forced wetting on structured surfaces plays a major role. Transfer and dosing of printing inks and coating liquids is controlled by the filling and emptying of the engraved patterns of the printing forms and cylinders with the respective liquids. It is known that surfactants play a significant role here [36].

We aim for a better understanding of how surfactants influence forced wetting on structured surfaces. Here we combine our previous work on the dewetting of surfactant solutions on flat surfaces [24–27,30,31] with the effects of pinning on surface structures [32–35]. For a good comparison, our samples have structured and unstructured regions side-by-side. This allows for a direct comparison of how the surface structure and surfactants influence dewetting. For this purpose, we mounted different custom-made gravure printing plates on a specially designed rotating drum setup, where the drum is half immersed in the liquid. The gravure cells in the printing plate act as pinning sites for the receding contact line. This pinning strongly influences the dewetting behavior. We find that, with increasing surfactant concentration, the dewetting behavior of rough surfaces approaches that of smooth surfaces. From this we conclude that hydrodynamic and Marangoni effects close to the contact line dominate over pinning effects for high enough dewetting speeds.

II. MATERIALS AND METHODS

A. Structured printing plates

We used custom-made gravure printing plates carrying a number of engraved cell raster areas with different cell geometries. The printing plates were provided by GT&W, Rödermark, Germany. The cells were mechanically engraved in a copper layer that has been galvanically deposited on 0.4 mm stainless-steel sheets. After removing the grates, the engraved surface was coated by approximately 5 μm of electrochemically deposited polished chromium, which was then hardened. The microstructures were analyzed with optical 3D surface microscopy [Nanofokus,

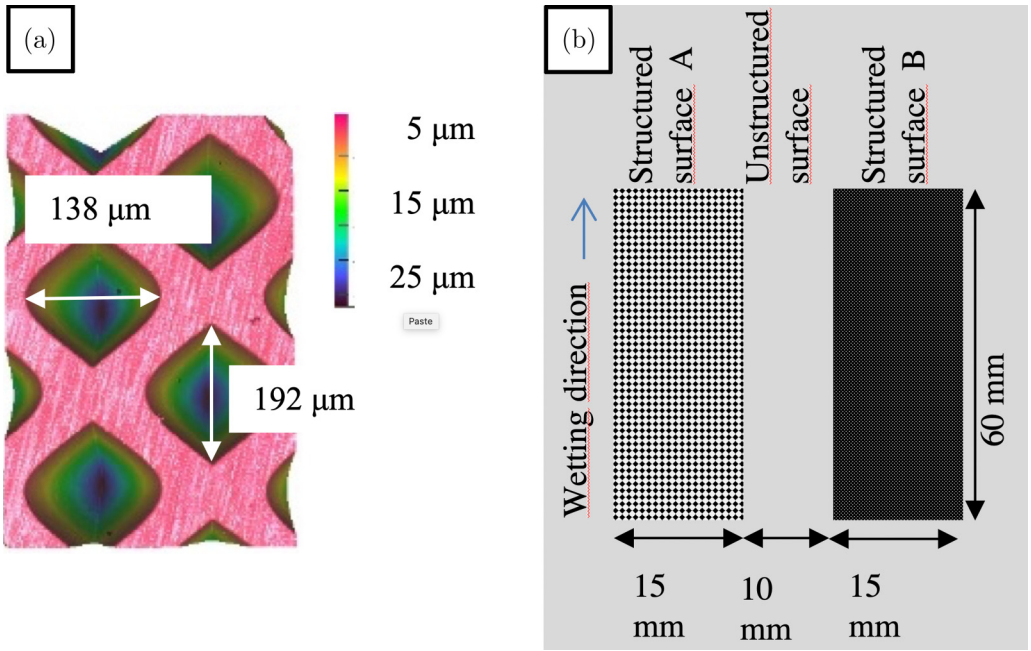

FIG. 1. (a) Optical 3D surface microscopy image of the structured surface B-25. (b) Sketch of the printing plates with two structured areas surrounded by unstructured surface. The orientation of the structured areas on the printing plate is also visible in Fig. 2(b).

50× magnification, Fig. 1(a)]. The measured dimensions of the gravures are summarized in Table I. The inner side walls of all gravure cells on all printing plates are inclined by an identical angle of about 20° relative to the flat surface.

There is also a roughness in the unstructured areas between the structured areas due to the production process. As measured with atomic force microscopy, the roughness is approximately $R_g \approx 35$ nm. The structured areas were $15 \times 60\,\mathrm{mm}^2$ in size and surrounded by an unstructured region [Fig. 1(b)]. Before using the plates for the wetting experiments, they were cleaned with ethanol and flowing ultrapure water.

TABLE I. Properties of the different areas on the printing plate. The labels reflect the distance between the neighboring gravure cells and their depth.

	Gravure cell dimensions			Distance between cells	
Label	x (μm)	y (μm)	Depth (μm)	x (μm)	y (μm)
B-7	85	45	7	262	262
B-9	98	62	9	262	262
B-13	117	84	13	262	262
B-25	192	138	25	262	262
S-4	46	31	4	218	212
S-7	63	49	7	218	212
S-9	82	68	9	218	212
S-19	135	121	19	218	212

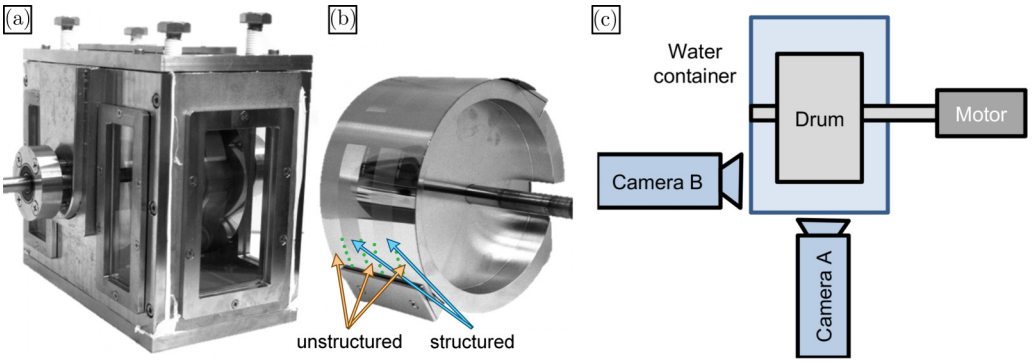

FIG. 2. (a) Photograph of the rotating drum setup. (b) Photograph of the drum with a printing plate mounted on the outer curved surface of the drum. The structured areas on the printing plate are visible by their stronger scattering of light, as indicated by the arrows. (c) Sketch of the experimental setup. Camera A is used for the height difference measurements, while camera B is used for the contact angle measurements.

Due to the production process, structured and unstructured areas thus chemically consist of the same material (electronically deposited chromium), and they can be assumed to have the same wetting properties. In the experiments, we used the unstructured areas as an internal reference to analyze the influence of the structure on the dewetting behavior.

B. Rotating drum setup

The rotating drum setup consists of a stainless-steel drum that is placed in a closed stainless-steel container [Fig. 2(a)]. Seven windows allow for optical observation of the advancing and receding contact lines. The inside of the container has a height of 150 mm, a length of 170 mm, and a depth of 90 mm. The windows are mounted at the front and back of the container, one at the top and two at every side of the drum axis. The container is made watertight using Teflon tape in every joint. In this way, we avoid any contamination of the liquid due to the sealing and allow for a thorough cleaning of the setup. The axis of the drum is sealed using gland packing sealing rings, made of Teflon. All measurements are carried out in a water-saturated atmosphere. After filling the container with the solution, we rotate the drum for at least 20 min to allow the air to be saturated with water vapor. To avoid surfactant transfer along the liquid surface from the receding to the advancing side, the container was filled to the axis of the drum [27], which corresponds to 1 L of liquid.

The cylindrical drum has a diameter of 120 mm, a width of 60 mm, and we have the option of mounting different kinds of flat bendable or flexible plates on the cylinder [Fig. 2(b)]. In this work, the above-described gravure printing plates were mounted on the drum. The drum is connected to a motor to vary the velocity of the printing plates between 0.1 and 100 mm/s. This motor allows a smooth motion of the drum. We use four different motors equipped with suitable gearings to cover one decade in velocity per motor. For comparison, measurements on a smooth surface were performed, where a drum with a spherical segment geometry (coated with polystyrene) such as that described in Ref. [24] was used.

We observed the receding contact line with a high-speed camera (Photron, Fastcam SA-1); see Fig. 2(c). The camera was equipped either with a 2× magnification objective with a working distance of 35 mm and an illumination through the objective (for contact line observation, camera position A), or with a 12× magnification objective with a working distance of 300 mm and back light illumination (for contact angle observation, camera position B). Typical frame rates varied between 250 and 500 frames per second. Since the printing plates only allow bending in one direction, i.e., they take a cylindrical shape upon bending, side view imaging of the contact line is difficult. The rotating cylinder is blocking part of the view field of the side-view objective. This

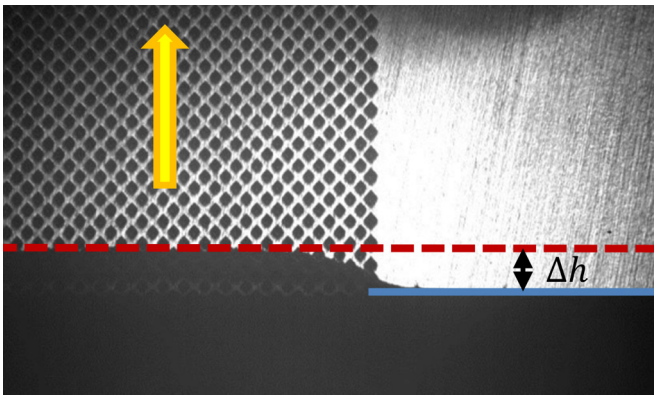

FIG. 3. Image of the contact line. The red dashed line marks the contact line on the structured surface and the blue solid line marks that on the unstructured surface. The difference between these is defined as the height difference Δh (black arrow). The yellow arrow indicates the direction of motion of the surface.

limits the optical resolution in the side view. Additionally, the unstructured and the structured areas are both along the optical path in the side view. Consequently, the menisci of the structured and unstructured parts overlap on side-view images, and contact angles cannot reliably be measured for the structured areas using side-view imaging. It is only possible to measure the contact angle on the unstructured regions of the printing plates.

Instead we measured the height difference Δh of the contact line on the structured and unstructured areas as a function of dewetting speed (Fig. 3). This height difference gives a direct measure of the changes in wetting properties due to the surface structures. As we will discuss later, this gives only indirect access to the overall height of the meniscus above the level of the unperturbed water surface.

C. Surfactant solution

We used solutions of the anionic surfactant sodium 1-decanesulfonate (S-1DeS) in ultrapure water. S-1DeS was purchased from Sigma-Aldrich and used without further purification. The ultrapure water was prepared by using an Arium® pro VF/UF& DI/UV (Sartorius) at a resistivity of 18.2 MΩ cm. All used concentrations are below the critical micelle concentration (CMC) of S-1DeS, i.e., the surfactant is molecularly dissolved in water in the form of single molecules, and no formation of aggregates is expected. The CMC of S-1DeS was measured with a Wilhelmy plate tensiometer (Dataphysics, DCAT 11EC) to be 38.5 mmol/L. At lab temperature, the surface tensions of the used solutions were measured to be as follows: 72.1 mN/m (S-1DeS concentration 0% of the CMC), 60.3 mN/m (15% CMC), 55.3 mN/m (30% CMC), and 49.7 mN/m (45% CMC) [24].

D. Measurement procedure

For cleaning before the experiment, the whole setup was rinsed overnight with flowing tap water and then immediately rinsed with flowing ultrapure water for 1 h to avoid calcification in the setup. To ensure the absence of water-soluble impurities in the setup, we systematically used ultrapure water as the first wetting liquid. Only when the measured values for contact angle and meniscus height did not change over an interval of half an hour of continuous measurements was the setup considered to be clean.

We measured the height difference Δh for all surfaces first for pure water and then for increasing surfactant concentration. This was done by successively adding the corresponding amount of surfactant. After each addition of surfactant, the solution was stirred for at least 20 min by rotating

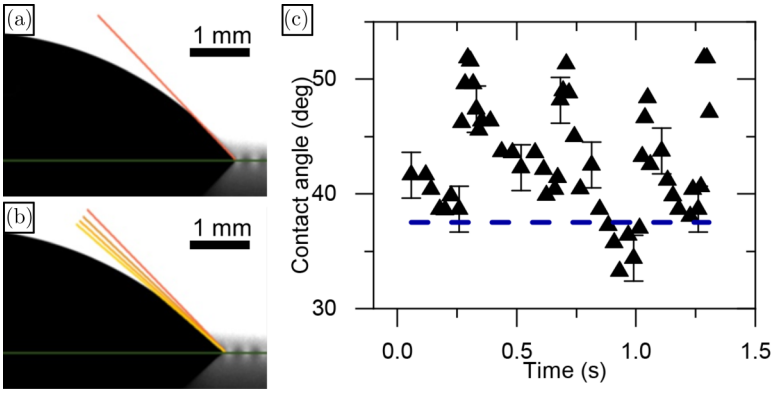

FIG. 4. Receding contact angle oscillation of a deflating drop on the B-25 surface. During deflation of the drop, the contact line moves to the left. (a) Contact angle on the flat part of the structured surface. (b) Due to pinning at the corner of the gravure cell, the contact angle changes while the drop moves over a gravure cell. The lines show the variation of the contact angle. (c) The contact angle variation during the movement of the contact line over the structured surface. Oscillations are due to pinning at the gravure cells. The contact angle varies by more than 15°. The dashed line is the contact angle on the smooth surface. The measurement error can be estimated to approximately 3°, as indicated in the plot.

the drum at 100 mm/s. S-1DeS was added stepwise to achieve concentrations of up to 45% of the critical micelle concentration (45% CMC).

III. RESULTS AND DISCUSSION

A. Pure water

1. Static contact angles

To measure the static contact angle on the printing plate, a drop of 10 μL water was placed (using an OCA 35 contact angle measuring device, DataPhysics). When inflating and deflating the drop, pinning of the contact line happened at the rims of the gravures of the printing areas. Due to this pinning, the quasistatic advancing and receding contact angle depends on the exact position of the contact line on the printing plate. For the receding contact angle, we observed variations of more than 15° while the contact line receded quasistatically (Fig. 4 for the B-25 surface). Typically, the contact line is pinned at a corner of a gravure cell. Therefore, the contact angle decreases while being pinned at the edge of the gravure cell and increases after jumping to the next row of gravure cells. This pinning phenomenon at edges is well known and described, e.g., in Refs. [17,37].

Due to these pinning effects, it is important to take all measurements at a specific instant while the contact line moves over the printing plate. In the rest of the paper, we systematically took the measurements just before the contact line jumped from one row of gravure cells to the next row. As we already discussed above (Sec. II B), side-view imaging to measure the contact angle on the structured part of the printing plate is not conclusive. For this reason, we used the height difference Δh between the structured and unstructured part as the primary parameter for the characterization of the dynamic wetting (Fig. 3).

2. Dynamic measurements

For all different kinds of structures used in this work, the height difference Δh increases with increasing velocity (Fig. 5). While moving the plate out of the liquid container, the contact line is pinned at the top edges of the gravures until it unpins for all gravures in one line almost simultaneously. We systematically evaluated the height difference just before the contact line

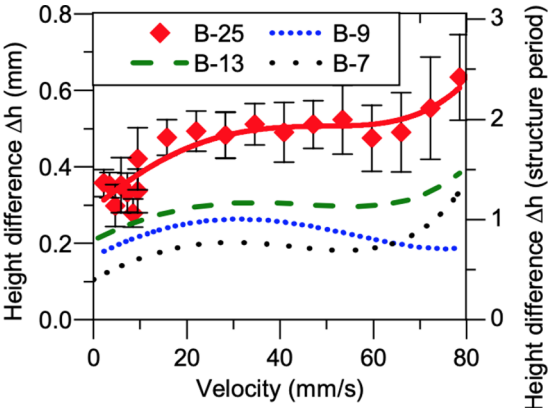

FIG. 5. Measured height difference Δh of the contact line for water between neighboring structured and unstructured parts of the printing plate (see Fig. 3 for the definition of Δh). The experiments were performed on a printing plate with 262 μm × 262 μm distances between the gravure cells. The red diamonds represent the structured area with the deepest gravures. The dashed lines are guides to the eye for the data with smaller gravures (compare Table I). The error bars represent the standard deviation of ten independent measurements.

unpins. At a specific velocity (e.g., for the surface B-25 20 mm/s, red diamonds in Fig. 5) the height difference reaches a plateau and further increases only for velocities above approximately 70 mm/s. The increase at higher velocities is associated with instabilities of the contact line. In that case, the contact line is not straight anymore but starts to buckle. This instability of the contact line is the first insinuation of the film formation that is observed at velocities above 80 mm/s. Therefore, no measurements are possible for speeds higher than 80 mm/s. For surfaces with shallow gravures (e.g., B-7), Δh in this plateau regime is about the center-to-center distance between the gravure cells. For the surfaces with deeper gravures (e.g., B-25) the plateau value of Δh amounts to more than twice this distance.

This implies that with increasing structure depth and width on the surface, the influence of the structures on the dewetting of water increases. Since the inclination of the side walls is independent of the cell size (Sec. II A), the variations in the height difference cannot be explained by a possible influence of the slopes of the side walls of the gravure cells. According to the standard pinning model [38], only the slope of the side walls but not the size of the gravure should influence pinning. We conclude that additional effects are involved, e.g., eventually slight but systematic changes in the local curvature of the rim of the gravures or by hydrodynamic effects induced by the emptying of the gravure cells (Sec. IV B).

As discussed above, direct optical determination of the dynamic receding contact angle on the structured areas is not easily possible. To overcome this limitation and to compare our results with previous experiments [23], we adopted the following strategy. We first measured the contact angle on the unstructured part of the surface. In regions with no structured areas along the line of sight, this is possible in side view. The measurement results of the contact angle on the smooth part of the surface are shown in Fig. 6(a) as violet open-squared symbols. Due to suboptimal optical conditions, the uncertainty of the contact angle measurement is somewhat increased compared to the spherical segment drum [39]. The contact angle on the smooth surface decreases with increasing velocity.

To deduce the contact angle on the structured parts of the surface, we used the fact that the shape of the meniscus follows the static shape for distances large compared to the slip length as well as the intermediate length scale [40]. Since we perform optical measurements with a resolution of around 100 μm, this is true for all our data. The height h_u of the contact line over the unperturbed liquid level [Fig. 6(b)] can be calculated by [41]

$$\gamma \sin\theta + \tfrac{1}{2}\varrho g h_u^2 = \gamma. \tag{1}$$

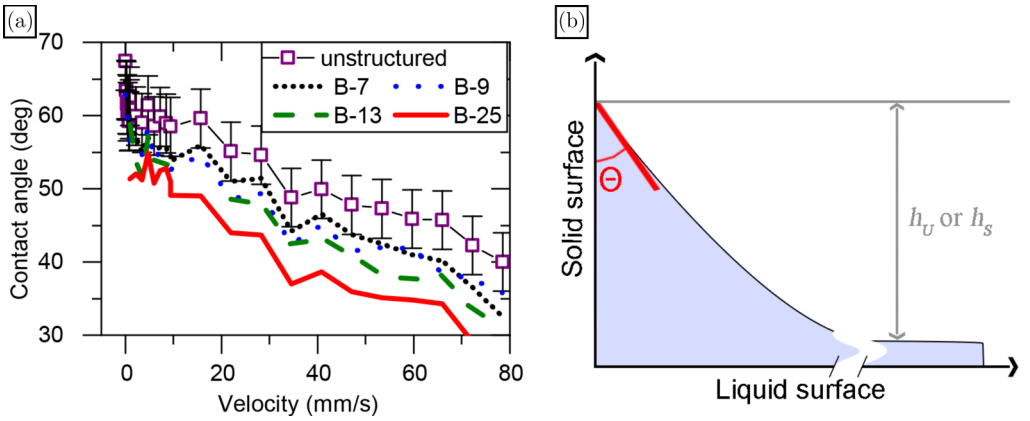

FIG. 6. (a) Measured receding contact angles (opened squares) of water on different surfaces. To calculate the contact angle on the structured part of the plate, Eqs. (1) and (2) were used. Here, we used a surface tension of 72 mN/m and a density of 998.2 kg/m^3. For better visibility, the error bars are only shown for the unstructured surface. For the structured surfaces, the error is ±6°. (b) Height of the meniscus over the unperturbed liquid level. The x-axis is broken to sketch the whole meniscus shape.

In this expression, γ is the surface tension of the liquid, θ is the contact angle, ϱ is the density of the liquid, and g is the gravitational acceleration. Using Eq. (1), we can calculate the height of the contact line over the unperturbed liquid level for the unstructured surface. By adding the height difference Δh between the unstructured part and the different structured areas [Eq. (2)], we can calculate the height of the contact line over the unperturbed liquid level on the structured areas h_s,

$$h_s = h_u + \Delta h. \tag{2}$$

Entering this value of h_s in Eq. (1) instead of h_u, we obtain an estimate of the contact angle θ on the structured parts as well [Fig. 6(a), lines without symbols]. In Fig. 4 we show that the receding contact angle actually depends on the relative position of the contact line to the gravures. We measured the minimal receding contact angle in the stick-slip motion on the structured surfaces at the moments when the contact line unpins (Fig. 4). The receding contact angle decreases with increasing velocity as well as with increasing structure depth on the surface (Fig. 6).

B. Surfactant solutions

To figure out the influence of surfactants on the dewetting of structured surfaces, we used concentrations of 0%, 15%, 30%, and 45% of the critical micelle concentration of S-1DeS, with a surface tension of 72.1, 60.3, 55.3, and 49.7 mN/m, respectively. As in the pure water case, we measured the height difference Δh for increasing velocities until the contact line started to become unstable, i.e., for velocities up to the crossover to film formation. As in the pure-water case, the height difference Δh first increases with increasing velocity and then reached a plateau Δh_{pl} [Fig. 7(a)]. However, as shown in Fig. 7(b), the height difference decreases with increasing surfactant concentration. Similar to [24,26,27], the film formation velocity as well as the contact angle decrease with increasing surfactant concentration [Fig. 7(c)]. The change in the contact angle increases with increasing surfactant concentration. This behavior is similar for all kinds of measured surfaces and comparable with the measurements of the same surfactant on a smooth surface [24] [Fig. 7(d)].

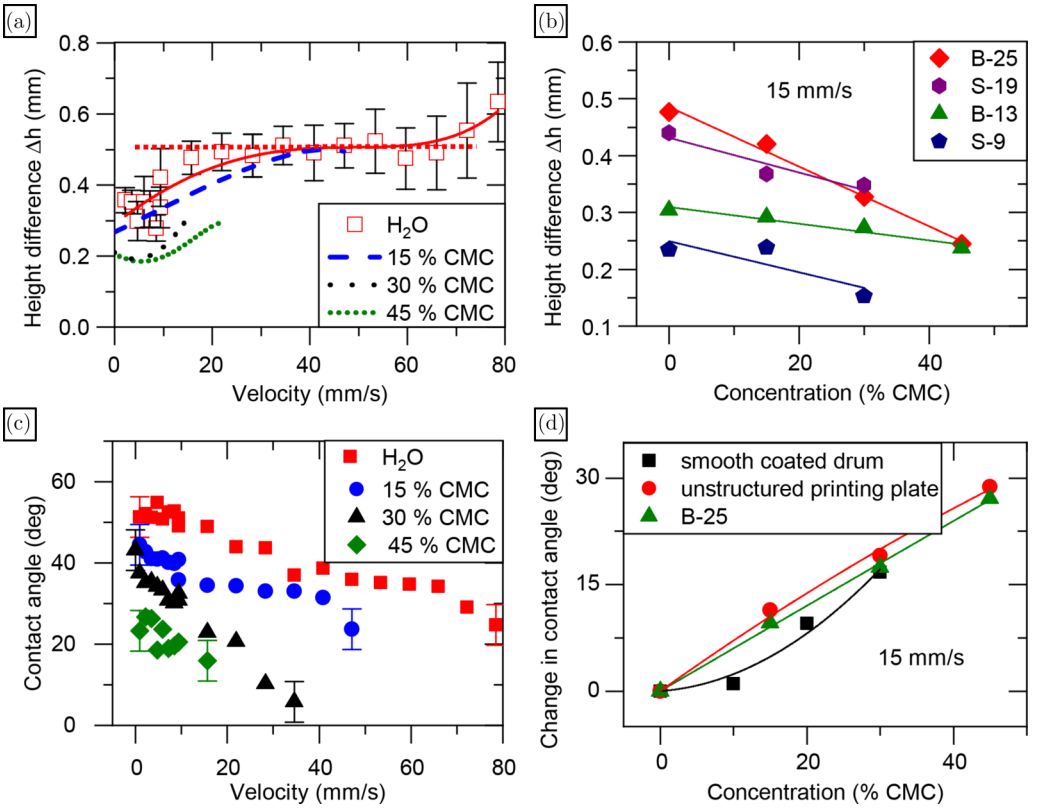

FIG. 7. (a) Measured height difference of the contact line on the structured and unstructured part on the printing plate B-25 for different surfactant concentrations. The concentration varies from 0% to 45% of the critical micelle concentration of S-1DeS. The red dotted line illustrates the height difference plateau Δh_{pl}. The error bars are obtained from ten independent measurements. (b) Change in the height difference of the contact line on different structured plates for different concentrations at a velocity of 15 mm/s. The lines are guides to the eye. (c) Calculated contact angle based on Eqs. (1) and (2) on the surface B-25. The error bars are similar for all concentrations. (d) Comparison of the change in the contact angle due to the addition of S-1DeS on the smooth part of the printing plate (red circles) and the structured surface B-25 (green rectangles) with the data published in Ref. [24] (black squares). The lines are guides for the eye.

IV. HYDRODYNAMIC CONSIDERATIONS

The height of the meniscus and the dynamic receding contact angle differ between unstructured and structured areas of the printing plate [Figs. 6 and 7(a)]. In all tested cases, these differences clearly decreased with increasing surfactant concentration [Fig. 7(b)]. Additionally, there are differences between the data measured on the smooth drum and the structured surfaces at low speeds and low surfactant concentrations [Fig. 7(d)]. For high surfactant concentrations, these differences tend to vanish. In an earlier work, some of us have shown that the dynamic receding contact angle follows hydrodynamic models at high enough dewetting speeds [24]. In summary, these experimental results indicated that the higher the contact line velocity and the higher the surfactant concentration, the more the dewetting seems to be dominated by hydrodynamic effects (e.g., Marangoni effects) and not by processes very close to the contact line, e.g., pinning of the contact line.

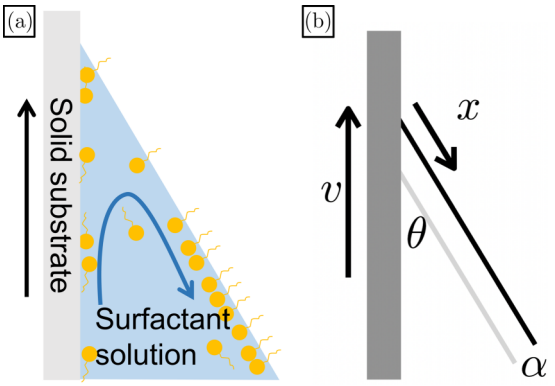

FIG. 8. (a) Sketch of the process close to the three-phase contact line in the presence of surfactants. The size of the surfactant molecules is not to scale (see the main text for details). Part (b) illustrates the definition of the quantities used in the scaling arguments.

A. Surfactant-induced flow

For an explanation of this behavior, we extend the model described earlier in Refs. [24,26]. A sketch of the processes that this model is based on is shown in Fig. 8. As expected by various hydrodynamic models [14–16], close to the substrate, the liquid moves with the solid surface toward the contact line. At the contact line the liquid changes its direction and flows along the liquid surface away from the contact line. This flow profile has been verified experimentally [24]. Correspondingly, close to the contact line a fresh surface is continuously generated. Two mechanisms are possible to bring the surface concentration of the surfactant in equilibrium with the bulk of the liquid. Either surfactant molecules adsorbed to the substrate are transferred to the fresh liquid-air interface at the contact line, or surfactant molecules from the bulk of the liquid diffuse to the liquid-air interface. Presumably, the adsorption of the surfactant at the solid surface is so strong (due to an electrostatic attraction between the surface and the surfactants) that no significant number of them can be transferred at the contact line to the liquid interface. For this reason, we assume that the dominating equilibration mechanism of the surface concentration of surfactant molecules is diffusion. As sketched in Fig. 8, this leads to a region of lower surface concentration close to the contact line. The size of this region depends on two characteristic length scales that describe the equilibrium conditions and the advection-diffusion dynamics.

In equilibrium, one can compare the surfactant concentration at the surface and in the bulk. A characteristic length scale α is the thickness of a liquid layer that contains as many surfactant molecules per unit area as the liquid-air interface. The thickness of this layer can be estimated using the Gibbs adsorption isotherm $\Gamma = -\frac{c}{2RT}\frac{d\gamma}{dc}$ and a linear dependence of the surface excess $\Gamma = \alpha c$ on the bulk concentration [26]. Here, c is the bulk surfactant concentrations, R is the ideal gas constant, and T is the absolute temperature. With an integration of the Gibbs adsorption isotherm between $c = 0$ and the CMC, one obtains

$$\Delta\gamma = 2\alpha RT \times \mathrm{CMC},, \tag{3}$$

where $\Delta\gamma$ is the surface tension difference between pure water and the surface tension at the CMC. For the S-1DeS, we measured a CMC of 38.5 mM and a surface tension of 39.7 mN/m at the CMC. This gives $\alpha \approx 180\,\mathrm{nm}$. This length scale is much smaller than the size of the gravure. But it is also much larger than molecular length scales, like the size of the surfactant molecules, or length scales of the molecular motion at the contact line, like slip lengths or hopping distances. α is in fact a length scale at which hydrodynamic arguments can be assumed to hold. To refill the freshly generated surface with surfactant molecules, all the molecules from a region of $x = 2\alpha/\tan\theta$ are

needed. The factor 2 is due to the assumed triangular shape of the region close to the contact line. Close to a receding contact line, the surface concentration of surfactant molecules is no longer in equilibrium in a region of at least this size close to the contact line. Due to the reduced surface concentration of surfactant in this region, gradients in the surface tension (and thus Marangoni stresses) build up. A higher surface tension is expected close to the contact line versus far away from it. The corresponding Marangoni stress slows down the flow close to the free surface. Note that the physical basis of the above argument (especially concerning the mentioned length scales) is the conservation of the surfactant. The total amount of the surfactants on the surface and in the bulk is conserved.

To equilibrate the surface concentration of surfactant with its bulk concentration, diffusion transports surfactant molecules to the liquid-air interface. This diffusion is approximately perpendicular to the streamlines of the hydrodynamic flow. The characteristic time scale can thus be estimated by the diffusive time scale

$$\tau_D = \frac{\alpha^2}{2D}, \tag{4}$$

with the diffusion coefficient of the surfactant $D = 6.98 \times 10^{-10}\ \mathrm{m}^2/\mathrm{s}$. We obtain $\tau_D \approx 2.3\ \mu\mathrm{s}$. This timescale has to be compared to the advective timescale τ_A over $x = 2\alpha/\tan\theta$, $\tau_A = 2\alpha/(v\ \tan\theta)$, where v is the contact line speed. The ratio between these timescales suggests the relative importance of both processes. For velocities at which the advective time scale τ_A is shorter than the diffusive time scale τ_D, the region of nonequilibrium surface tension is expanded, because diffusion is not fast enough to replenish the liquid-air interface. By equating τ_A and τ_D, we obtain the following expression for this characteristic velocity:

$$v = \frac{4D}{\alpha \tan\theta} \tag{5}$$

For a typical contact angle of $\theta = 30^\circ$, we obtain $v_A \approx 26.9\ \mathrm{mm/s}$. This implies that for almost all velocities used in our experiments, the region of nonequilibrium surface tension is similar to $x = 2\alpha/\tan\theta$.

This concentration gradient along the liquid-air interface (along with the corresponding gradient in surface tension and Marangoni stress) has important consequences for the flow profile. Close to the contact line, this Marangoni stress counteracts the flow along the free surface away from the contact line [Fig. 8(a)]. This situation bears some similarities to the stagnant caps of bubbles rising in surfactant solutions [42,43], where Marangoni stresses along the bubble surface also influence the flow profile around the bubble.

In our case, however, the detailed flow profile in the vicinity of the contact line is still unknown. Quantitative statements are thus not possible. Based on the current and previous experimental results, we suggest the following picture. The contact line velocity is held constant in our experiments. Previously, we concluded that the presence of surfactants effectively leads to an increased contact line friction for receding contact lines [24]. The above argument shows that, for high enough contact line speeds, an extended region of reduced flow velocity (away from the contact line) of the free surface is expected. As the contact line speed is constant, the inflow into the contact line region is constant. Since the outflow along the free surface is reduced, the outflow is effectively more "confined" in the inner part of the wedge between substrate and liquid surface close to the contact line. This "confinement" is expected to lead to steeper velocity gradients and thus a higher viscous dissipation close to the contact line. With increasing surfactant concentration, the Marangoni stress along the free surface is expected to increase, as is the "confinement" of the flow and the additional dissipation. For this reason, the influence of the surfactant on the flow increases with increasing concentration.

This Marangoni-induced dissipative mechanism close to the contact line adds to the other mechanism that contributes to the dynamic contact angle. The experimental results of this and previous works [24,26] show that, at high enough velocities, the effectively increased dissipation

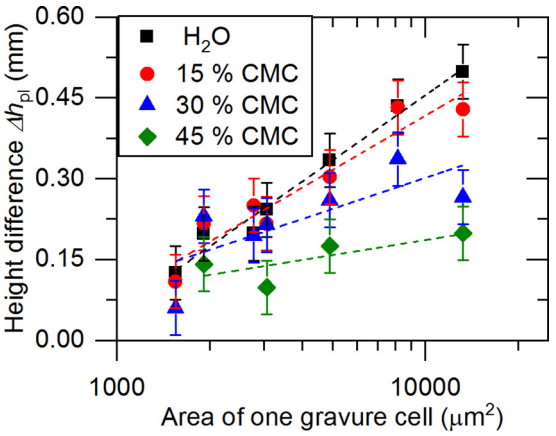

FIG. 9. Measured height difference of the plateau Δh_{pl} [see Fig. 7(a)] for all different kinds of surfaces employed. The height difference is plotted over the area of one gravure cell for both distances between the gravure cells. With increasing surfactant concentration, the influence of the structure decreases. The bars represent the standard deviation of the data points in the plateau. The dashed lines are guides to the eye.

close to the contact line due to Marangoni stresses seems to dominate the motion of receding contact lines of surfactant solutions (see the discussion of Fig. 9 below). In our previous work, we observed a crossover to a regime in which hydrodynamic models for dynamic receding contact angles are applicable.

B. Dependence on the characteristics of the surface structure

The effects of Marangoni stresses and pinning also show distinct differences, e.g., with respect to the velocity dependence and the dependence on the size of the gravure. The strength of the pinning at the gravure cells (as measured through the height difference Δh) depends on the size of the gravure [Fig. 7(b)].

A basic result of our measurements is the plateau in Δh plotted against the dewetting velocity. We compare the plateaus in Δh obtained for six different types of gravure cells (characterized by the gravure cell area) in Fig. 9. The plateau values [see Fig. 7(a)] are defined by calculating the average values of the data points between the initial rise of Δh and its final increase at the speed of film formation.

For pure water, the height difference Δh of the contact line increases with increasing size of the individual gravure cells (Fig. 9, black squares). Actually, for all surfactant concentrations, the data points follow on average an increasing curve when plotting them against the size of the individual gravure cells. This illustrates that the size (e.g., the area) of the gravure cell is more important than the area fraction. Actually, the area fraction does not scale with the area of the cells, because we used different spacings between the gravure cells. We note that choosing the area of the gravures is an arbitrary choice; any other geometric feature of the single gravures that measures their size (length, depth, volume, etc.) would lead to the same conclusion.

When adding surfactant, the influence of the structure on the wetting behavior decreases with increasing concentration (compare Sec. IV B). The higher the surfactant concentration, the smaller is the influence of the surface structure on the dewetting process (Fig. 9). A similar effect has been observed in the contact angles that seem to converge to the same value independent of the surface structure for high enough surfactant concentrations (Fig. 7).

C. Emptying of the gravure cells

To rationalize why the height difference Δh exhibits a plateau in a certain velocity range, we had a closer look at the emptying behavior of single gravure cells. We imaged the process with a higher

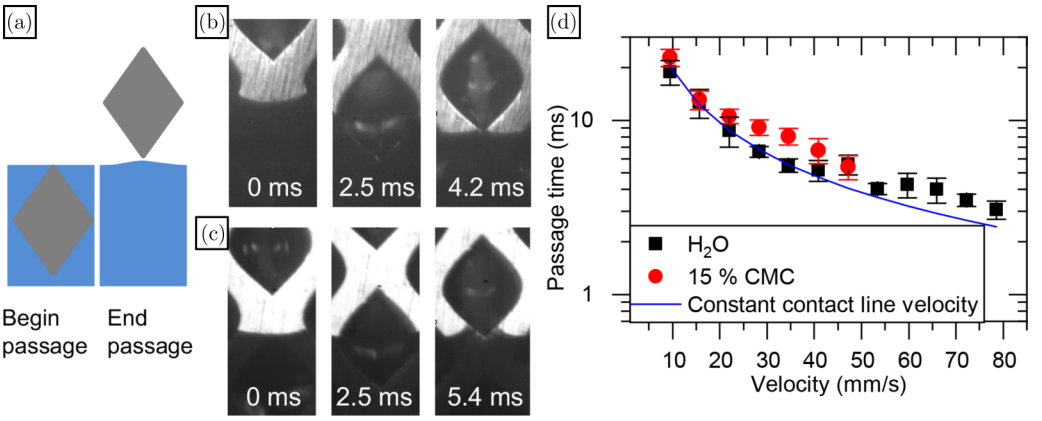

FIG. 10. Parts (a)–(c) show the emptying process of a gravure cell. While (a) defines the passage time as the time the contact line needs from the top corner of the gravure cell to depin from the bottom corner, (b) depicts the emptying for pure water, and (c) depicts the emptying for a solution with 15% CMC of S-1DeS. The first frame in (b) shows the appearance of the gravure cell at the contact line, the second one the middle of the emptying process (after 2.5 ms), and the third frame the depinning of the contact line from the bottom of the gravure cell. Part (d) presents the passage time for one gravure cell with and without surfactant for different velocities. The solid blue line indicates the passage time for a constant contact line velocity.

magnification objective (50×), which allows us to observe the emptying of single gravure cells (Fig. 10). The passage time is defined as the time the contact line needs from the top corner of the gravure cell to depin from the bottom corner [Fig. 10(a)]. We measured the passage time for different velocities with and without surfactants in the solution. The passage time decreases with increasing velocity. For water, the passage time follows the prediction of a constant contact line velocity up to a velocity of 40 mm/s. Above this velocity, it increases above this value. This indicates that the contact line moves with different speeds over pinning sites, gravures, and the region between gravures [Fig. 10(d)]. This variation of the passage time correlates with the plateau in the height difference measurements (Fig. 7). Similarly, for surfactant solutions the passage time decreases with increasing velocity. Above a velocity of 10 mm/s we observe deviations of the passage time from the values derived based on the given surface velocity. This indicates that the emptying behavior of a single gravure cell differs for surfactant solutions and pure water. We attribute this difference to the additional dissipative mechanisms close to the contact line discussed above.

It is not yet clear whether the gravure cells will be completely empty after the passage of the contact line. Therefore, we had a closer look at the emptying mechanism. Due to optical reflection and the inclined side walls of the gravure cells, it is not possible to unambiguously decide if the gravure cells are completely empty after the contact line has depinned.

To see if the emptying of the gravure cells is complete, we used an infrared camera (Infatec, VarioCam HD) to image the cells after emptying (Fig. 11). We placed a 300 μL water drop on a slightly tilted printing plate. The drop starts to move over the surface with an average velocity of approximately 10 mm/s. On the unstructured part, the temperature of the printing behind the drop is similar to the temperature in front of the drop. However, on the structured part, the temperature behind the drop is lower than that in front of it. We attribute this temperature decrease to the evaporation of water that was left in the gravures after the passage of the contact line. The cells did not empty completely during the emptying/passage time. Note that the liquid left in the gravures pinches-off from the liquid in the bath. This process bears some similarities to the motion of contact lines over chemical heterogeneities, as, e.g., discussed in Ref. [44].

To overcome the optical limitations and to see in detail what happens in the gravure cells, we used a structured SU-8 substrate with circular holes (diameter 48 μm, depth 11 μm, distance between the

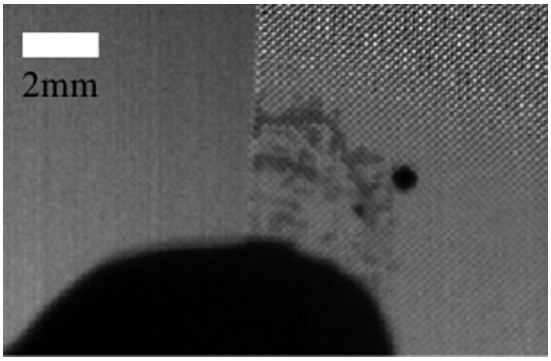

FIG. 11. IR image of a moving drop. The left side shows an unstructured surface, the right side the structured surface B-25. Darker regions emit less IR radiation (e.g., they are colder or reflect less IR radiation) than brighter regions.

centers 100 μm), and we investigated the receding contact line on this surface. A drop is placed on the surface, and the volume is reduced by a syringe pump. Due to the decreasing volume, the contact line moves over the surface and the receding contact line can be imaged. The average velocity of the contact line achieved that way was around 0.3 mm/s. Comparable to the movement of the receding contact line on the printing plates, the contact line pins at the edge of the holes and slips to the next hole afterward. After the contact line has depinned from the cells, there is still liquid inside the cells. More precisely, the evaporation of the water remaining in the cells typically takes 0.9 s.

Since all imaged cells of the SU8 surface show an incomplete emptying process, and additionally the IR images of a moving drop over the structured printing plate show a difference in temperature, we conclude that some residual liquid remains inside the cells of the printing plate. This picture suggests that the measured passage time depends on the average contact line velocity as well as on the hydrodynamics of the emptying process. When the contact line depins from a (only partially emptied) gravure cell, the remaining liquid has to pinch off from the contact line. This leads to an additional hydrodynamic resistance related to the contact line motion. Especially, the pinch-off process of the contact line from the liquid remaining in the gravure cell can depend on the volume in the gravure cell. Thus, this additional hydrodynamic effect contributes to the pinning of the contact line and, especially, to the dependence of the pinning on the size of the gravure cells that was observed (Figs. 7 and 9).

V. CONCLUSION

On structured surfaces, the dynamic contact angle decreases with increasing surfactant concentration. At a certain dewetting speed, not a defined three-phase contact line but a continuous liquid film is formed. This speed, at which the contact line starts to become unstable and begins to buckle, decreases with increasing surfactant concentration. This behavior is qualitatively similar to the behavior on smooth surfaces [23,24].

Usually structured surfaces show a strong pinning of the contact line. Here, we have shown in dynamic situations that the importance of pinning due to surface structures decreases with increasing surfactant concentration. With increasing surfactant concentration, Marangoni stresses close to the contact line increase and start dominating the effect of pinning.

We demonstrated that the individual gravure cells are not completely empty after the contact line has passed over them. A small amount of liquid remains inside the cells. The remaining liquid has to pinch-off from the liquid in the receding contact line. This adds a dynamic mechanism of pinning that depends on the liquid volume in gravure cells, i.e., on their size.

ACKNOWLEDGMENTS

The authors thank Noemí Encinas García for the preparation of the SU8 surface and Ilka Hermes for the AFM measurements. We kindly acknowledge the financial support by the German Research Foundation (DFG) within the Collaborative Research Centre 1194 "Interaction of Transport and Wetting Processes," Projects A02 (Auernhammer, Hardt), A06 (Henrich), and C03 (Butt).

[1] N. Gao *et al.*, How drops start sliding over solid surfaces, Nat. Phys. **14**, 191 (2017).
[2] Y. Zheng, X. Gao, and L. Jiang, Directional adhesion of superhydrophobic butterfly wings, Soft Matter **3**, 178 (2007).
[3] D. Bonn *et al.*, Wetting and spreading, Rev. Mod. Phys. **81**, 739 (2009).
[4] S. Kumar, Liquid transfer in printing processes: liquid bridges with moving contact lines, Annu. Rev. Fluid Mech. **47**, 67 (2015).
[5] T. W. Walker *et al.*, Enhanced particle removal using viscoelastic fluids, J. Rheol. (1978–present) **58**, 63 (2014).
[6] V. Andreev *et al.*, Silicon-wafer cleaning with aqueous surfactant-stabilized gas/solids suspensions, J. Electrochem. Soc. **158**, H55 (2011).
[7] F. Zhang *et al.*, The removal of deformed submicron particles from silicon wafers by spin rinse and megasonics, J. Electron. Mater. **29**, 199 (2000).
[8] W. Kern, The evolution of silicon wafer cleaning technology, J. Electrochem. Soc. **137**, 1887 (1990).
[9] J. H. Snoeijer and B. Andreotti, Moving contact lines: scales, regimes, and dynamical transitions, Annu. Rev. Fluid Mech. **45**, 269 (2013).
[10] A. Marmur, Solid-surface characterization by wetting, Annu. Rev. Mater. Res. **39**, 473 (2009).
[11] P. G. De Gennes, Wetting: statics and dynamics, Rev. Mod. Phys. **57**, 827 (1985).
[12] T. D. Blake and J. M. Haynes, Kinetics of liquid-liquid displacement, J. Colloid Interface Sci. **30**, 421 (1969).
[13] T. D. Blake, The physics of moving wetting lines, J. Colloid Interface Sci. **299**, 1 (2006).
[14] J. Eggers and H. A. Stone, Characteristic lengths at moving contact lines for a perfectly wetting fluid: the influence of speed on the dynamic contact angle, J. Fluid Mech. **505**, 309 (2004).
[15] R. G. Cox, The dynamics of the spreading of liquids on a solid surface. Part 1. Viscous flow, J. Fluid Mech. **168**, 169 (1986).
[16] O. V. Voinov, Hydrodynamics of wetting, Fluid Dyn. **11**, 714 (1976).
[17] D. Quéré, Wetting and roughness, in Annu. Rev. Mater. Res., Annu. Rev.: Palo Alto **38**, 71 (2008).
[18] K. Dieter-Kissling, H. Marschall, and D. Bothe, Numerical method for coupled interfacial surfactant transport on dynamic surface meshes of general topology, Comput. Fluids **109**, 168 (2015).
[19] F. Schönfeld and S. Hardt, Dynamic contact angles in CFD simulations, Comput. Fluids **38**, 757 (2009).
[20] X. Wang, L. Chen, and E. Bonaccurso, Comparison of spontaneous wetting and drop impact dynamics of aqueous surfactant solutions on hydrophobic polypropylene surfaces: scaling of the contact radius, Colloid Polym. Sci. **293**, 257 (2015).
[21] D. Y. C. Chan, E. Klaseboer, and R. Manica, Dynamic deformations and forces in soft matter, Soft Matter **5**, 2858 (2009).
[22] O. Manor *et al.*, Hydrodynamic Boundary Conditions and Dynamic Forces Between Bubbles and Surfaces, Phys. Rev. Lett. **101**, 024501 (2008).
[23] Y. Amarouchene, G. Cristobal, and H. Kellay, Noncoalescing Drops, Phys. Rev. Lett. **87**, 206104 (2001).
[24] F. Henrich *et al.*, Influence of surfactants in forced dynamic dewetting, Soft Matter **12**, 7782 (2016).
[25] D. Truszkowska *et al.*, Forced dewetting dynamics of high molecular weight surfactant solutions, Colloids Surf. A **521**, 30 (2017).
[26] D. Fell *et al.*, Influence of surfactant concentration and background salt on forced dynamic wetting and dewetting, Langmuir **27**, 2112 (2011).

[27] D. Fell *et al.*, Influence of surfactant transport suppression on dynamic contact angle hysteresis, Colloid Polym. Sci., **291**, 361 (2013).
[28] H.-J. Butt, K. Graf, and M. Kappl, *Physics and Chemistry of Interfaces* (Wiley-VCH Verlag GmbH & Co. KGaA, Weinheim, Germany, 2003).
[29] H. C. Mayer and R. Krechetnikov, Landau-Levich flow visualization: Revealing the flow topology responsible for the film thickening phenomena, Phys. Fluids **24**, 052103 (2012).
[30] M. Anyfantakis *et al.*, Time-dependent dynamic receding contact angles studied during the flow of dilute aqueous surfactant solutions through fluorinated microtubes, Chem. Lett. **41**, 1232 (2012).
[31] K. S. Varanasi and S. Garoff, Unsteady motion of receding contact lines of surfactant solutions: The role of surfactant re-self-assembly, Langmuir **21**, 9932 (2005).
[32] N. T. Chamakos *et al.*, Droplet spreading on rough surfaces: Tackling the contact line boundary condition, Phys. Fluids **28**, 022105 (2016).
[33] J. Wang *et al.*, Surface structure determines dynamic wetting, Sci. Rep. **5**, 8474 (2015).
[34] J. F. Joanny and M. O. Robbins, Motion of a contact line on a heterogeneous surface, J. Chem. Phys. **92**, 3206 (1990).
[35] J. A. Lee, J. P. Rothstein, and M. Pasquali, Computational study of viscoelastic effects on liquid transfer during gravure printing, J. Non-Newtonian Fluid Mech. **199**, 1 (2013).
[36] B. Thompson, *Printing Materials: Science and Technology* (Pira International, Leatherhead, UK, 2004).
[37] S. Herminghaus, M. Brinkmann, and R. Seemann, Wetting and dewetting of complex surface geometries, Annu. Rev. Mater. Res. **38**, 101 (2008).
[38] S. Herminghaus, Roughness-induced non-wetting, Europhys. Lett. **52**, 165 (2000).
[39] T. F. Eibach *et al.*, Measuring contact angle and meniscus shape with a reflected laser beam, Rev. Sci. Instrum. **85**, 013703 (2014).
[40] T. S. Chan, T. Gueudré, and J. H. Snoeijer, Maximum speed of dewetting on a fiber, Phys. Fluids **23**, 112103 (2011).
[41] A. W. Neumann, Contact angles and their temperature dependence: thermodynamic status, measurement, interpretation and application, Adv. Colloid Interface Sci. **4**, 105 (1974).
[42] Z. He and C. Maldarelli *et al.*, The size of stagnant caps of bulk soluble surfactant on the interfaces of translating fluid droplets, J. Colloid Interface Sci. **146**, 442 (1991).
[43] S. S. Dukhin *et al.*, Dynamics of rear stagnant cap formation at the surface of spherical bubbles rising in surfactant solutions at large Reynolds numbers under conditions of small Marangoni number and slow sorption kinetics, Adv. Colloid Interface Sci. **222**, 260 (2015).
[44] G. Deleon, M. Fermigier, J. H. Snoeijer, and B. Andreotti, Relaxation of a dewetting contact line. Part 2. Experiments, J. Fluid Mech. **604**, 55 (2008).